ENGINEERING

Polymer-modified halide perovskite films for efficient and stable planar heterojunction solar cells

Lijian Zuo,[1,2] Hexia Guo,[1] Dane W. deQuilettes,[3] Sarthak Jariwala,[4] Nicholas De Marco,[1,2] Shiqi Dong,[1] Ryan DeBlock,[1] David S. Ginger,[3] Bruce Dunn,[1] Mingkui Wang,[5]* Yang Yang[1,2]*

The solution processing of polycrystalline perovskite films introduces trap states that can adversely affect their optoelectronic properties. Motivated by the use of small-molecule surfactants to improve the optoelectronic performance of perovskites, we demonstrate the use of polymers with coordinating groups to improve the performance of solution-processed semiconductor films. The use of these polymer modifiers results in a marked change in the electronic properties of the films, as measured by both carrier dynamics and overall device performance. The devices grown with the polymer poly(4-vinylpyridine) (PVP) show significantly enhanced power conversion efficiency from 16.9 ± 0.7% to 18.8 ± 0.8% (champion efficiency, 20.2%) from a reverse scan and stabilized champion efficiency from 17.5 to 19.1% [under a bias of 0.94 V and AM (air mass) 1.5-G, 1-sun illumination over 30 min] compared to controls without any passivation. Treating the perovskite film with PVP enables a V_{OC} of up to 1.16 V, which is among the best reported for a $CH_3NH_3PbI_3$ perovskite solar cell and one of the lowest voltage deficits reported for any perovskite to date. In addition, perovskite solar cells treated with PVP show a long shelf lifetime of up to 90 days (retaining 85% of the initial efficiency) and increased by a factor of more than 20 compared to those without any polymer (degrading to 85% after ~4 days). Our work opens up a new class of chemical additives for improving perovskite performance and should pave the way toward improving perovskite solar cells for high efficiency and stability.

INTRODUCTION

Hybrid perovskite solar cells (HPSCs) show great potential as a renewable energy source due to their exceptional optoelectronic properties and the possibility of low-cost solution processing to reduce manufacturing cost and energy input (*1*–*6*). Starting from 3.8% in 2009 (*7*), the state-of-the-art HPSC power conversion efficiency (PCE) has surged to a certified state-of-the-art value of more than 22.1% within a short time span, owing to the recent advancements in interface modification (*8*–*11*), morphology manipulation (*12*–*17*), composition engineering (*18*–*21*), etc. It has been shown that an ultimate efficiency of more than 30% and a maximum V_{OC} of 1.33 V can be theoretically achieved for the methylammonium lead tri-iodide ($MAPbI_3$) systems (*22*). However, charge recombination via nonradiative channels, such as defects or trap states, constitutes a major energy loss mechanism, which sets the upper limits for practically achievable PCE of $MAPbI_3$ solar cells (*23*). Thus far, as literature reports, the highest efficiency of a $MAPbI_3$ HPSC is around 20% with a V_{OC} of ~1.11 V (*24*, *25*). Thus, further boosting the HPSC toward their ultimate device efficiency relies on both fundamental understanding and advanced strategies to suppress nonradiative energy loss channels, such as charge recombination via defect states in the bulk or interfaces of the HPSC.

Defect states are well known to have a significant effect on device performance in many thin-film semiconductor photovoltaic technologies (*26*–*28*). For instance, abundant trap states can exist at the grain boundaries in semiconductors such as a polycrystalline Si thin film, where dangling bonds form deep defect states and significantly affect charge recombination and transport in photovoltaic devices (*29*). Because HPSCs are processed from solution at low temperature, defects in the polycrystalline perovskite films are likely unavoidable. These defects can lead to nonradiative energy loss, decreasing radiative efficiency, which may reduce the V_{OC} and device performance below the Shockley-Queisser limit. For example, the grain boundaries of perovskite films show optoelectronic properties that are different from the bulk and exhibit shorter charge carrier lifetime and weaker photoluminescence (PL) intensity (*30*). Studies using Kelvin probe force microscopy and conductive atomic force microscopy have shown that the grain boundaries and the bulk have different electrical potentials (*31*) and that grain boundaries have faster ion migration than the bulk (*32*). However, contrary results have also been reported to claim benign or even beneficial grain boundaries (*31*, *33*–*35*). Notably, the chemical composition at the grain boundaries varies depending on the processing methods, which can be the most plausible explanation to the debate on the effects of grain boundaries (*20*, *25*, *36*). Through theoretical studies, Haruyama *et al.* investigated the influence of different terminations at the grain boundaries and interstitials and found that the grain boundary composition terminated by either the iodide or the ammonium ion can significantly affect the optoelectronic properties of the perovskite grains (*37*–*39*). Tailoring the chemical composition of perovskite films can be an effective strategy to passivate defects and improve optoelectronic properties and overall device performance, which has been successfully demonstrated via small molecules, such as pyridine (*40*), thiophene (*40*), tri-*n*-octylphosphine oxide (*41*), and fullerenes (*42*, *43*). However, the design rules for the selection of an efficient passivating agent for high HPSC device performance are lacking. Moreover, passivation of perovskite films, especially within the bulk film, using long-chain polymers that might coordinate with Pb^{2+} sites has rarely been reported (*44*), likely due to the challenges in film fabrication in the presence of a high–molecular weight polymer. However, compared to small molecules, polymers can form more stable and reliable interactions with the perovskite grains and could conceivably cross-link grains to improve film stability, as has been proposed for alkylphosphonic acid ω-ammonium chlorides (*45*).

Here, we successfully demonstrate a highly efficient and stable HPSC, which exhibits a champion reverse-scanned efficiency of

---

[1] Department of Materials Science and Engineering, University of California, Los Angeles, Los Angeles, CA 90095, USA. [2] California NanoSystems Institute, University of California, Los Angeles, Los Angeles, CA 90095, USA. [3] Department of Chemistry, University of Washington, Box 351700, Seattle, WA 98195–1700, USA. [4] Department of Materials Science and Engineering, University of Washington, Seattle, WA 98195, USA. [5] Wuhan National Laboratory for Optoelectronics, Huazhong University of Science and Technology, Luoyu Road 1037, Wuhan 430074, P.R. China.
*Corresponding author. Email: mingkui.wang@hust.edu.cn (M.W.); yangy@ucla.edu (Y.Y.)

20.2% [averaged efficiency of 18.8 ± 0.8% and stabilized efficiency of 19.1%, with bias of 0.94 V, under AM (air mass) 1.5-G, 1-sun illumination] and long shelf lifetime, by chemically tailoring the perovskite film composition. We explore using polymers bearing different functional groups and propose that the binding interaction between the perovskite and the polymers is a key parameter affecting the passivation. The highest V_{OC} of the HPSC by poly(4-vinylpyridine) (PVP) passivation reaches 1.16 V (1.14 ± 0.02 V) with the planar $MAPbI_3$ system [E_g of ~1.63 eV from electroabsorption spectroscopy (*46*); absorbing edge of 795 nm], and thus, a champion small V_{OC} deficit (0.47 V; $E_g/e\text{-}V_{OC}$) is achieved in the $MAPbI_3$ system, which is also among the lowest of all types of perovskite solar cells (*47*). In addition, the HPSC with PVP passivation shows less hysteresis, a stable efficiency of up to 19% at a bias of 0.94 V under AM 1.5-G, 1-sun illumination, and an improved shelf lifetime of up to 90 days, retaining more than 85% of the initial efficiency. The influence of different polymers on the carrier dynamics and trap-state densities of perovskite films is studied via transient PL, transient photovoltage (TPV)/transient photocurrent (TPC) decay, and electronic impedance spectroscopy (IS) measurements.

RESULTS

Figure 1A shows the chemical structure of the polymers and a schematic of their possible interaction with perovskite. The branched polyethyleneimine (b-PEI), PVP, and polyacrylic acid (PAA) polymers were selected because of their possibility for different chemical interactions with the perovskite film: The b-PEI is rich in (possibly protonated) amino groups, PVP is rich in Lewis base pyridine groups, and PAA is rich in carboxylic acid groups. The lone electron pairs at the N or O of b-PEI, PVP, and PAA can be delocalized to the 6p empty orbits of Pb^{2+} to form coordination bonds with different bonding strengths (*48*, *49*). The bonding energy between the polymers and the $MAPbI_3$ was estimated using density functional theory (DFT) (see the Supplementary Materials for the calculation method details in the vacuum state), and the absorption energy for amino, pyridine, and carboxylic groups to the $MAPbI_3$ crystalline slab is calculated to be 51.88, 37.70, and 15.71 kJ/mol, respectively (Table 1). The strong interactions between the polymer and the perovskite can also be confirmed by the observation after adding the polymers into the perovskite precursor solutions (fig. S1A). For example, blending the b-PEI solution into the PbI_2/methylammonium iodide (MAI) solution immediately forms a precipitate at the bottom of the vial, and all the lead component is absorbed by the b-PEI, rendering the upper liquid colorless. A gelation structure is formed by adding the PVP polymer (fig. S1B), but the solution remains clear with PAA. From the DFT calculation (vacuum state), we predicted that the interaction between the polymers and the perovskite could be a dative bond between the Pb^{2+} and functional groups on the polymer (that is, pyridine and amino), and formation of complex molecules of perovskite and polymers can also be expected.

Unfortunately, the strong interactions between the polymers and the perovskite precursor make it challenging to form a homogenous perovskite films with these polymers via the conventional one-step or two-step method. To resolve this problem, here, we use an interdiffusion method (*50*), as illustrated in Fig. 1B. The key to develop the polymer-coordinated perovskite films is the formation of a mesoporous PbI_2 layer (Fig. 1D), which is created by a slow growth process (*51*). That is, the half-dried PbI_2 (spin-coated for 20 s) substrates were kept in a glass petri dish for 15 min, during which the transparent PbI_2 turned cloudy, consistent with the formation of a mesoporous structure, as has been previously reported. The polymers were then blended with the MAI in isopropanol (IPA) solution to form perovskite films with different polymers. We propose that during the perovskite crystallization step, induced by dripping the MAI/polymer solution onto the films, the micropores in the PbI_2 films allow the infiltration of the polymers into the PbI_2 film (Fig. 1E). After MAI/polymer dripping, the perovskite films containing polymers were formulated via thermal annealing. In the conventionally processed PbI_2 films, the films show homogeneous texture, and most of the polymers are expected to segregate at the perovskite surface due to the "filter" effect of the pinhole-free homogeneous film (Fig. 1C), which might form a barrier for charge extraction.

The existence of polymers and the formation of different coordination bonds within the perovskite film can be probed by Fourier transform infrared spectroscopy (FTIR). The samples for FTIR measurement were prepared with the same procedure as the device fabrication but with a higher polymer content (10:1) to increase the signal. A NaCl substrate was used to hold the films for the measurement. The main spectral feature to be considered in the PVP film is the deformation modes (*52*) of the pyridine rings at 1597 cm^{-1}, as shown in Fig. 1F. The same absorption feature is observed in the PVP-perovskite films, but the feature peak moves to 1604 cm^{-1}, presumably due to the increased rigidity (*53*). This shift would be consistent with the formation of coordination bonds by sharing the lone electron pair on the N to the empty 6p orbit of Pb^{2+}. A distinct absorption peak appeared at 1711 cm^{-1} for the intrinsic PAA film (*53*), and this peak is shifted to 1722 cm^{-1} due to coordination with the perovskite (Fig. 1G), where the lone electron pair on the carboxylic group is delocalized to the empty orbit of Pb^{2+}. Because large amounts of ammonium groups exist in the perovskite film, it is very difficult to distinguish the feature absorptions of b-PEI and MA^+ (fig. S2). However, the interaction between the perovskite and the b-PEI polymer should be strong according to the DFT calculations. The location of the polymers in the perovskite film was further examined with glow-discharge optical emission spectroscopy (GDOES) measurements, which is a technique used to measure the chemical composition as a function of depth with parts-per-million sensitivity (*54*). PAA was selected as a model due to the existence of O atoms, which should not be present in the $MAPbI_3$ perovskite. Thereafter, the existence of PAA can be traced by probing the oxygen content in the perovskite film. As shown in Fig. 1H, the O signal intensity in the perovskite film with PAA is greater than the O baseline intensity observed in several bare perovskite films throughout the film. Although sample-to-sample variations in adventitious O_2 and H_2O could also account for the different O baseline of the PAA films, we neglected the possibility because we found that the increased O baseline far exceeded the sample-to-sample variation for similar batches of bare perovskite film processed and measured under identical conditions (fig. S3). These results confirm that the polymers were incorporated throughout the film with mesoporous PbI_2. The film morphology of the perovskite film with and without different polymer modifications was also examined by scanning electron microscopy (SEM). As shown in fig. S4, all the perovskite films with and without polymers exhibit similar morphology, with large grain size around 700 nm and smooth surface without any pinholes. The unchanged crystallinity of perovskite films with and without polymers was confirmed by the x-ray diffraction (XRD) patterns, which are similar for the perovskite with and without different polymers (fig. S5). Therefore, we conclude that incorporation of polymers into the perovskite films via the interdiffusion method has little influence on the film morphology but that it is likely that the polymers are being incorporated at some level throughout the depth of the films.

HPSC devices were fabricated using the perovskite films with and without polymer incorporation. Figure 2A shows the device architectures.

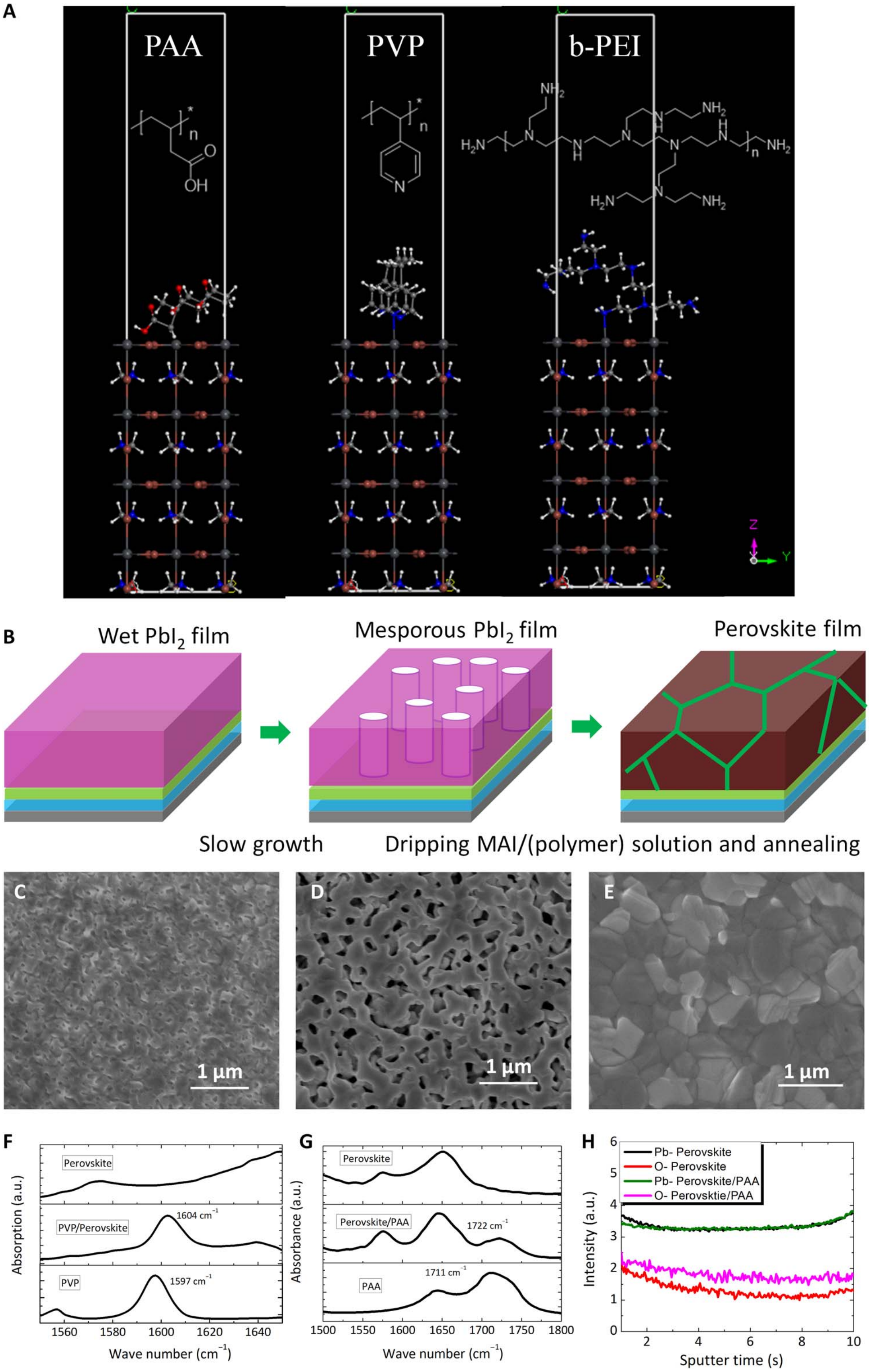

Fig. 1. Polymer-passivated perovskite films. (**A**) Chemical structures of b-PEI, PAA, and PVP. (**B**) Schematic diagram for incorporating the polymer into the perovskite films. SEM images of (**C**) homogeneous PbI_2 film without slow growth, (**D**) mesoporous PbI_2 film with slow growth, and (**E**) perovskite film processed from slowly grown PbI_2 with PVP polymer. (**F**) FTIR spectra of perovskite, PVP, and perovskite/PVP films. a.u., arbitrary units. (**G**) FTIR spectra of perovskite, PAA, and perovskite/PAA films. (**H**) GDOES measurement of perovskite and perovskite/PAA films.

Table 1. Absorption energy and carrier dynamic properties of different functional group–modified perovskite films.

Polymer	Functional group	Absorption energy (kJ/mol)	Averaged PL lifetime (ns)	Carrier lifetime (μs)	Carrier transport time (μs)
—	—	—	96	1.35	0.75
PAA	Carboxylic acid	15.71	178	1.95	0.75
PVP	Pyridine	37.70	281	2.69	0.72
b-PEI	Amino	51.88	11	1.01	0.85

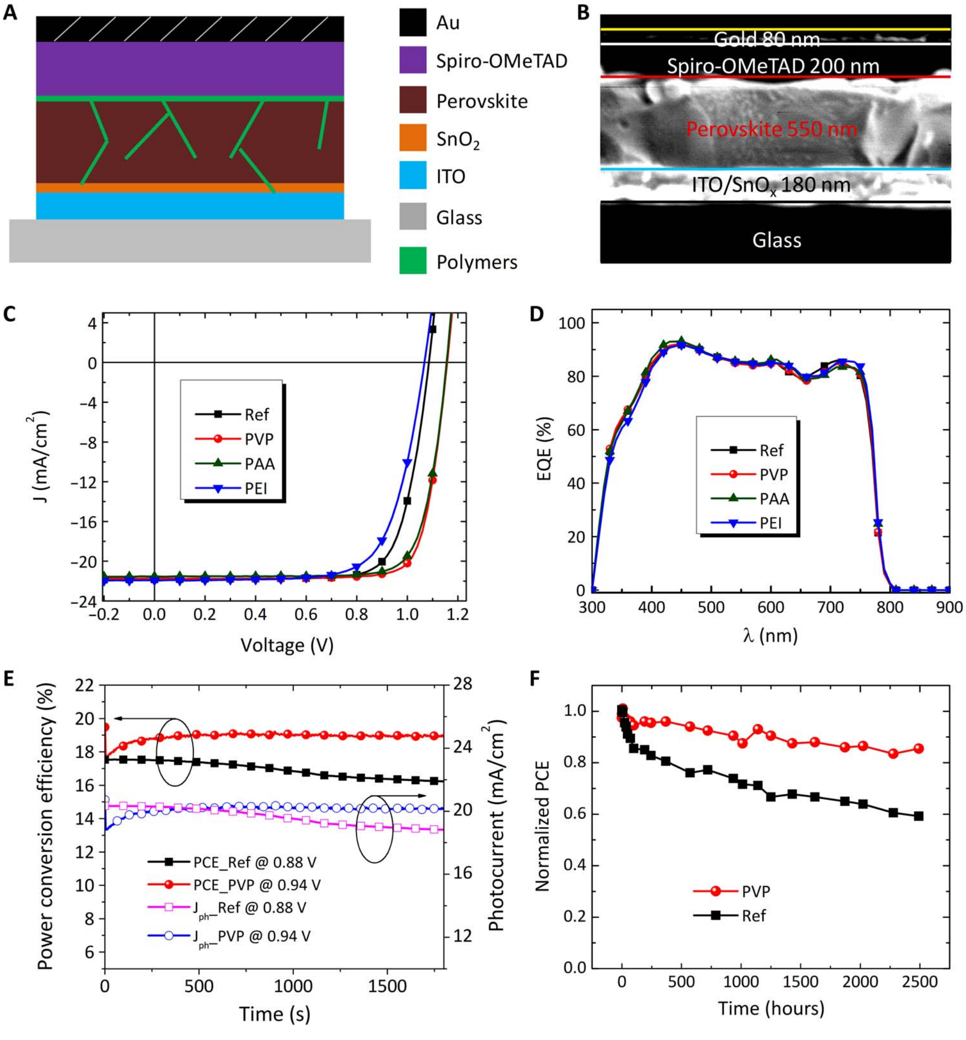

Fig. 2. $CH_3NH_3PbI_3$ solar cell devices with different polymer converted from microporous PbI_2. (**A**) Schematic diagram of the device architecture. (**B**) Cross-sectional image of the solar cells. ITO, indium tin oxide. (**C**) *I-V* characteristics, (**D**) EQE spectra, (**E**) steady-state output power, and (**F**) shelf time of the solar cells with and without PVP treatment.

SnO_2 (*11*) and 2,2′,7,7′-tetrakis(*N*,*N*-di-4-methoxyphenylamino)-9,9′-spirobifluorene (Spiro-OMeTAD) (*6*) were applied as the electron transport layer and hole transport layer (HTL), respectively. Cross-sectional images of the devices, shown in Fig. 2B, show a homogeneous pinhole-free 550-nm perovskite film fully covered by a 200-nm Spiro-OMeTAD layer. The current-voltage relation (*I-V*) characteristic curves of the HPSC devices with and without different polymers are shown in Fig. 2C, and the corresponding device parameters are summarized in Table 2. The best HPSC without passivation shows a high reverse-scanned PCE of 18.02% (averaged efficiency of 16.9 ± 0.7% from more than 70 devices), with a V_{OC} of 1.09 V, a J_{SC} of 21.82 mA/cm^2, and a fill factor (FF) of 0.76. With PVP treatment, the champion HPSC shows a significant improvement in reverse-scanned PCE to 20.23% (averaged efficiency of 18.8 ± 0.8% from more than 90 devices), where the highest

Table 2. Device parameters of polymer-modified perovskite solar cells. RS, reverse scan; FS, forward scan.

Polymer		J_{SC} (mA/cm^2)	V_{OC} (V)	FF (/)	PCE (%)
—	RS	21.82 (21.51 ± 0.21)	1.09 (1.03 ± 0.04)	0.759 (0.709 ± 0.047)	18.05 (16.91 ± 0.68)
	FS	21.83 (21.47 ± 0.23)	1.03 (0.98 ± 0.02)	0.690 (0.61 ± 0.051)	15.52 (14.12 ± 0.97)
PAA	RS	21.53 (21.31 ± 0.19)	1.16 (1.14 ± 0.02)	0.794 (0.729 ± 0.042)	19.65 (17.94 ± 0.74)
	FS	21.59 (21.31 ± 0.20)	1.11 (1.08 ± 0.02)	0.767 (0.700 ± 0.049)	18.37 (16.84 ± 0.94)
PVP	RS	21.74 (21.52 ± 0.11)	1.15 (1.13 ± 0.02)	0.809 (0.737 ± 0.052)	20.23 (18.82 ± 0.84)
	FS	21.69 (21.36 ± 0.15)	1.13 (1.10 ± 0.02)	0.767 (0.711 ± 0.039)	18.80 (16.94 ± 0.84)
b-PEI	RS	21.94 (21.71 ± 0.13)	1.07 (1.00 ± 0.05)	0.710 (0.628 ± 0.057)	16.67 (15.8 ± 0.73)
	FS	21.87 (21.70 ± 0.12)	1.05 (0.95 ± 0.07)	0.657 (0.611 ± 0.035)	15.08 (13.87 ± 0.78)

V_{OC} is 1.16 V (averaged value of 1.14 ± 0.02 V), J_{SC} is 21.74 mA/cm^2, and FF is 0.81. This change represents a more than 10% improvement in PCE compared to the champion film without PVP; furthermore, the average device performance increased by 10%. Notably, the HPSC devices with PVP treatment reach a high V_{OC} of 1.16 V (fig. S6), which is the highest V_{OC} reported for MAPbI$_3$-based HPSC we are aware of to date. The ultrahigh V_{OC} enables an unprecedented low V_{OC} deficit of 0.47 V for the MAPbI$_3$ system, considering a band gap of 1.63 eV, as measured from electroabsorption spectroscopies [external quantum efficiency (EQE) response edge of ~795 nm (fig. S7)] (*46*). The low V_{OC} deficit obtained from HPSC devices with PVP passivation suggests a significant suppression of nonradiative charge recombination, as will be discussed below. The influence of different amounts of PVP content on the device performance is also studied, and the *I*-*V* characteristic curves are shown in fig. S8. The best device performance is obtained when the PVP/MAI ratio is 1:1000 by weight %. Less PVP content will cause insufficient passivation, and excessive PVP can potentially cause charge transport problems. To investigate whether the improvement in PCE was due to the passivation in the bulk of the perovskite or only at the interfaces with HTL, we fabricated the HPSC device with a thin PVP polymer on top of the perovskite film. With PVP only present on top of the perovskite, the device performance showed only a small improvement in reverse-scanned PCE from 18.05% (averaged 16.9 ± 0.7%) to 18.61% (17.6 ± 0.5%, averaged from 15 devices) (fig. S9). This result implies that the incorporation of PVP into the bulk and/or its presence during the microporous film growth is critical to the observed performance enhancement.

The HPSCs also showed appreciable improvements with PAA treatment, where the highest reverse-scanned PCE of 19.64% (averaged value of 17.9 ± 0.7% from more than 50 devices) was achieved, with a J_{SC} of 21.53 mA/cm^2, a V_{OC} of 1.15 V, and an FF of 0.79. In contrast, however, the HPSC device made with b-PEI treatment exhibited a significant drop in performance, with the highest reverse-scanned PCE dropping to 16.67% (averaged value of 15.8 ± 0.7%, from over 50 devices), with a J_{SC} of 21.94 mA/cm^2, a V_{OC} of 1.07 V, and an FF of 0.71. Variation in device performance is also shown in the device histogram in fig. S10.

Figure 2D shows the external quantum efficiency of the HPSC with different polymers. The EQE profiles are similar for all the different films with the highest EQE of 93% at ~450 nm. The integrated J_{SC} from the EQE using the AM 1.5 reference spectra reaches 21.5 mA/cm^2, which is close to that from the *I*-*V* measurement (21.7 mA/cm^2; PVP-modified HPSC). The *I*-*V* hysteresis problem is typically observed in planar heterojunction HPSC (*54*, *55*), which casts doubt on the device efficiency obtained from *I*-*V* scan. The mechanism of *I*-*V* hysteresis is still under investigation, and it has been demonstrated that the hysteresis is most likely associated with the ionic nature of perovskite, such as ion migration (*56*–*58*). In our case, the HPSC device performance deviation between the forward and backward scan is also evaluated. As shown in fig. S11, all the HPSC devices show the *I*-*V* hysteresis problem to different extents. The device parameters with different scan direction and different polymers are summarized in Table 2. The HPSC device with no polymers shows a forward-scanned PCE of 15.52%, retaining 86% of the reverse-scanned efficiency (18.05%), but enhanced to 18.80% with PVP passivation, retaining 92% of the reverse-scanned efficiency (20.23%). The forward-scanned efficiency of PAA- and b-PEI–modified perovskite solar cells retained 93 and 90% of that from the reverse scan, respectively. It is evident that the hysteresis problem is alleviated with incorporation of polymers.

The appearance of hysteresis makes it hard to judiciously evaluate the device performance simply through the *I*-*V* curve scan (*55*–*58*). On the contrary, steady-state output power mimicking the real working condition of solar cells under a bias light and voltage is a more reliable method to characterize the authentic performance of HPSC (*18*). Figure 2E illustrates the steady-state output power of HPSCs under ambient conditions (20° to 25°C; relative humidity of 25 to 40%) under continuous AM 1.5-G, 1-sun illumination and a constant bias voltage. As shown, HPSCs without any polymer treatment show a maximum output power of 17.5 mW/cm^2 (or stabilized PCE of 17.5%) under 0.88 V and degrades to 16.2 mW/cm^2 after 30 min. The HPSC with PVP treatment exhibits a maximum output power of 19.1 mW/cm^2 (or stabilized PCE of 19.1%) under 0.94 V, and little drop is observed after 30 min (18.9 mW/cm^2). Note that the champion stabilized efficiency of 19.1% represents one of the highest among planar heterojunction MAPbI$_3$ HPSCs (*24*, *25*). These results verify the enhanced device performance and, moreover, the improved stability under working condition of an HPSC device with PVP passivation.

Furthermore, the shelf life stability of the HPSCs was also evaluated. The HPSC devices for shelf time stability tests were encapsulated by curable epoxy glue and a glass cover, stored in a glove box, and measured under ambient condition (20° to 25°C; relative humidity of 25 to 40%).

As shown in Fig. 2F, the HPSC without the PVP surface passivation degrades to 59% of the initial efficiency after 2500 hours, whereas the HPSC with PVP passivation retains more than 85% of the original efficiency after 2500 hours. We speculate that because the polymers can bind multiple interfaces, the improved working stability and shelf time can be possibly attributed to cross-linking of the grains, as has been proposed for treatment with alkylphosphonic acid ω-ammonium chlorides (*45*). It could also be that the polymer simply helps prevent access of water to the perovskite or that it actually reduces the mobility of some of the perovskite components (*44*). In any event, the origin of the improved lifetime is beyond the scope of this study but should prove an interesting topic for future investigation.

Next, the carrier dynamics of the perovskite films were investigated to gain more insight into the mechanism of HPSC device performance changes with the different polymer treatments. It has been demonstrated that charge recombination via nonradiative recombination is the most significant energy loss channel at carrier densities comparable to 1-sun illumination conditions (*23*). Notably then, Fig. 3A shows that the PL intensity increased by ~700% with PVP and by ~650% with PAA but dropped by 70% with b-PEI. These changes provide strong evidence that the polymer treatments are altering the nonradiative decay rates in a manner consistent with the observed changes in device performance: PVP and PAA treatments both result in increased PL (reduced nonradiative losses) and increased device performance, whereas b-PEI results in a decrease in PL (increased nonradiative losses) and a concomitant decrease in device performance.

In addition, we measured PL by exciting the samples from different sides, that is, the top surface of the perovskite film (front side) and the glass side (back side). As shown in fig. S12, the perovskite films processed from mesoporous PbI_2 and compact PbI_2 show similar PL intensity when excited from the top side and the glass side. For the perovskite/PVP films processed from compact PbI_2 (where we would expect the polymer to reside predominantly at the film surface), the PL intensity is significantly greater when excited from the perovskite/PVP side compared to when excited from the glass side. On the other hand, the perovskite/PVP film processed from mesoporous PbI_2 (where we hypothesize that the PVP will be able to penetrate the film thickness during growth) showed similar PL intensity when excited from either side. Because optical simulations show that excitation at 640 nm will be primarily absorbed by the first 250-nm perovskite layer, we interpret these results as evidence to support the hypothesis that the PVP treatment of the mesoporous PbI_2 films results in a change in the electronic properties throughout the entire film, whereas the compact film is only affected at the interface with the PVP.

We also measured the transient PL response of the perovskite films with different polymers. The fluence for the TRPL measurement is around 11 nJ/cm^2 with a frequency of 1 MHz, and the excitation density is around 10^{14} cm^{-3}. The PL transient data further support our proposal that films treated with PVP and PAA show improved optoelectronic properties with reduced levels of nonradiative recombination. As shown in Fig. 3B, the PL decays were fitted with a stretched exponential equation ($I = I_0 e^{-\left(\frac{t}{\tau_c}\right)^{\beta}}$) (*30*, *41*, *59*, *60*). The reference perovskite film without any polymer showed a characteristic PL lifetime of $\tau_c \sim 89 \pm 2$ ns and stretching exponent $\beta \sim 0.86 \pm 0.02$, which is consistent with literature (*59*). With the polymer treatments, the PL transient decays exhibit longer lifetimes and less dispersion in decay rates for PVP and PAA,

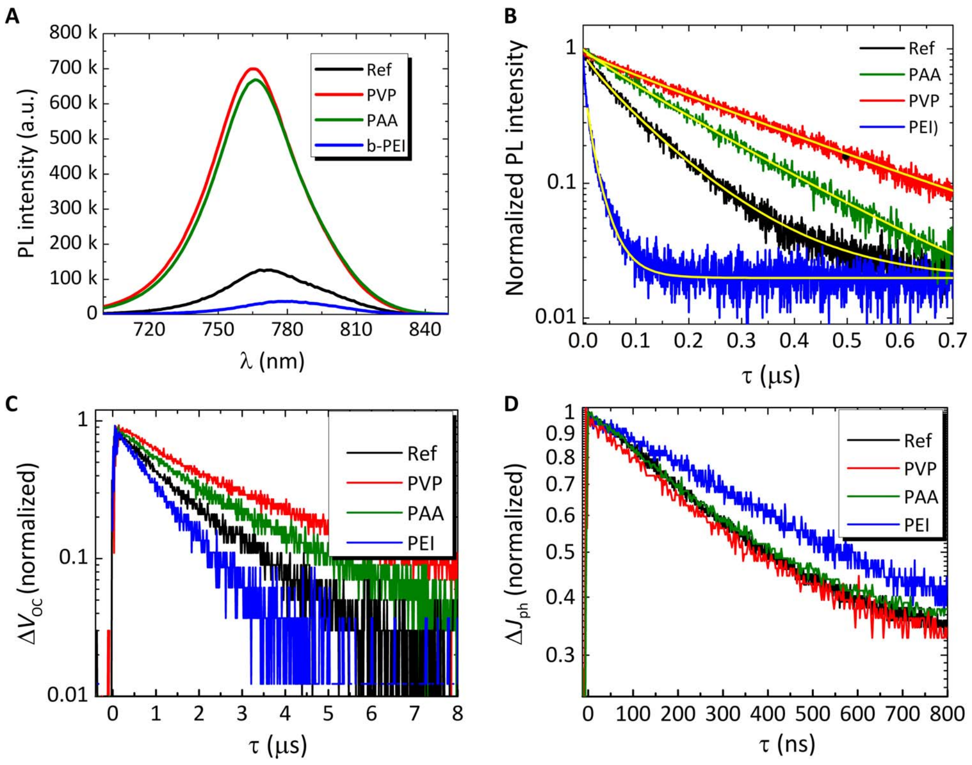

Fig. 3. Carrier dynamics. (**A**) PL intensity spectra and (**B**) time-resolved PL (TRPL) decay spectra of perovskite films with different polymer incorporation. The fluence for the TRPL measurement is around 11 nJ/cm^2, and the excitation density is around 10^{14} cm^{-3}. Yellow line represents the fitted curve using the stretched exponential function. (**C**) TPV and (**D**) TPC of perovskite solar cells with different polymers.

with $\tau_c \sim 275 \pm 3$ ns and $\beta \sim 0.95 \pm 0.02$ for PVP and $\tau_c \sim 172 \pm 1$ ns and $\beta \sim 0.93 \pm 0.01$ for PAA, and a reduction in lifetime and increased dispersion with b-PEI treatment, with $\tau_c \sim 8 \pm 0.3$ ns and $\beta \sim 0.66 \pm 0.01$. We calculated the average lifetime $\langle\tau\rangle$ of the stretched exponential distribution according to the equation $< \tau >= \frac{\tau_c}{\beta}\int_0^\infty x^{(1-\beta)/\beta} e^{-x} dx$. Following the equation, we report an averaged lifetime of 96, 281, 178, and 11 ns for control perovskite, perovskite/PVP, perovskite/PAA, and perovskite/b-PEI films, respectively. The increase in lifetime for PVP and PAA passivation indicates reduction in nonradiative recombination in the perovskite film, whereas the shortened lifetime for b-PEI suggests introduction of nonradiative recombination centers within the perovskite film, which is consistent with the PL intensity trends.

During the operation of a real HPSC device, photogenerated carriers are collected at electron and hole-collecting electrode interfaces, for example, Spiro-OMeTAD/perovskite (for holes) or SnO_2/perovskite (for electrons), and there exists the possibility for additional nonradiative decay pathways introduced by the electrode/perovskite interfaces (*61*). The separated photocarriers can either recombine via surface trap states or be swept out of the device for electrical power generation. In this scenario, the techniques of TPV and TPC decay can provide additional information about carrier dynamics during device operation. A bias light with intensity of around 1 sun is applied to follow the kinetics at carrier densities approximating those from the working condition of HPSCs, and a laser pulse (pulse width of 4 ns and a repetition frequency of 10 Hz) is used to generate small disturbance on V_{OC} (ΔV_{OC} of ~5 meV). The decay of TPV traces the fates of photocarriers at a small perturbation above open-circuit conditions, where the separated photocarriers mainly recombine via defect or trap states. Thereafter, the TPV lifetime, taken as the time at which a small photovoltage decays to $1/e$ of its peak intensity, can be extracted to learn about the charge recombination rate. As shown in Fig. 3C, the TPV lifetime of HPSC without any polymer passivation is ~1.35 μs and increases to 1.95 and 2.69 μs with PAA and PVP passivation, respectively. However, the carrier lifetime reduces to 0.9 μs with b-PEI incorporation. The elongated carrier lifetime of HPSC with PVP and PAA passivation is again consistent with our proposal that treatment with these polymers during growth reduces the density of defect states in the film. The decay of TPC is recorded under short-circuit condition, where the photocarriers swept out of the device can quickly recombine via the external circuit. The decay of TPC illustrates the photocarrier transit time across the bulk perovskite and the electrode interfaces. As shown in Fig. 3D, the photocarrier transit time in HPSC without any polymer passivation is ~0.75 ± 0.02 μs, and little change is observed with PAA (0.75 ± 0.02 μs) or PVP (0.72 ± 0.01 μs) passivation. However, the transit time becomes longer with b-PEI modification (0.85 ± 0.03 μs). We attributed the elongated transit time to the increased charge traps in the b-PEI–modified perovskite films, which decrease the effective carrier mobility. The TPV/TPC results are again broadly consistent with the conclusions from the PL measurements and, in turn, with the trends observed in device performance variation with different polymer treatments.

Electronic impedance measurements (fig. S13) were carried out to determine the origin of the difference in the photovoltage and FF upon polymer treatment. As shown in Fig. 4 (A and C), under the same V_{OC}, the devices with PAA and PVP demonstrated larger interfacial charge transfer resistances and longer lifetimes, being consistent with the photovoltaic performance for the two devices with higher V_{OC} and FF (*62*, *63*). This result has been confirmed by TPV decay measurements of the carrier lifetime shown in Fig. 3C. As shown in Fig. 4B, the capacitance

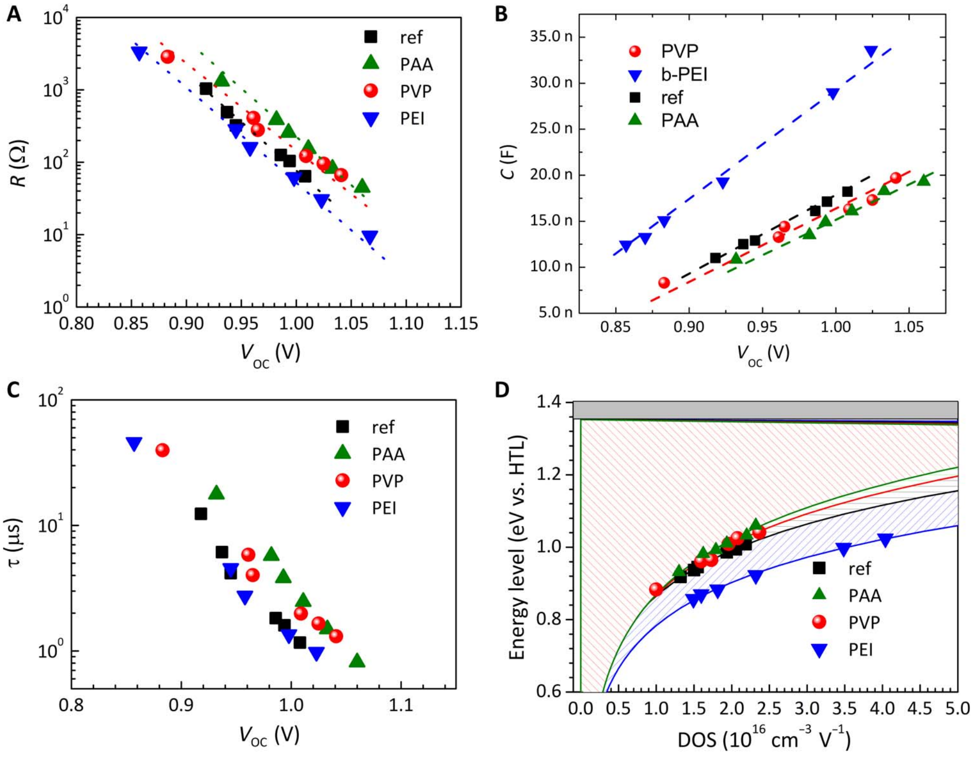

Fig. 4. Electronic IS measurements. Plots for (**A**) charge transfer resistance (*R*) and (**B**) the correlated capacitance (*C*), (**C**) lifetime (τ), and (**D**) DOS versus electron energy level in various devices.

C exhibits an exponential increase with V_{OC}. Therefore, the interfacial trap density of states [DOS; $\mathrm{DOS} = \frac{N_{t,0}}{k_B T_0} \exp(\frac{E_F - E_C}{k_B T_0})$, where $N_{t,0}$ is the total density of the localized state, and T_0 has the unit of temperature and reflects the width of the trap distribution function below the edge of the conduction band (E_C), a high value of T_0 implying a broad DOS] distribution function can be plotted as shown in Fig. 4D. Using an exponential function to fit the capacitance curves in Fig. 4B gives T_0 around 1649 K for the reference device, 1365 K for PAA-device, 1461 K for PVP device, and 1737 K for b-PEI device. The DOS in the range of ~10^{16} cm^{-3} indicates the high quality of the perovskite films investigated in this study. As shown in Fig. 4D, if we set a given DOS for four samples, then an increase of electron energy level can be observed in the order of b-PEI < reference < PVP < PAA. As schematically illustrated in Fig. 4D, a narrower DOS distribution suggests that PAA and PVP reduce the density of defects/trap states.

DISCUSSION

To summarize our experimental result, we demonstrate that the incorporation of polymer additives into the perovskite film is an effective strategy to improve both the device efficiency and the stability of perovskite solar cells. The mechanism regarding the device performance variations is attributed to the changes of trap states in the whole perovskite film with different polymers, as unveiled by the PL intensity, carrier dynamics, and impedance study. The variation in device performance and other optoelectronic properties is correlated to different interactions of the functional groups with perovskite (fig. S14), based on which possible rules guiding the passivating mechanism for perovskite is proposed. As shown, the perovskite solar cells show the best performance with the pyridine group, having a binding energy of 37.70 kJ/mol with Pb^{2+}. With low coordination energy (carboxylic group, 15.71 kJ/mol), the passivation effect becomes relatively weak but still shows significant improvement compared to the reference. Thereafter, coordination bonds, especially those with large binding energy with the perovskite film (or Pb^{2+}), would benefit the trap-state passivation. Defect states can possibly be passivated by chemical groups that donate electron density, likely by sharing lone electron pairs (*41*) presumably with the empty 6p orbitals of undercoordinated Pb^{2+} sites. The decrease in device performance with high–coordination energy b-PEI seemed to contradict with our conclusion. However, further analysis from proton nuclear magnetic resonance (^{1}H NMR) measurements (fig. S15) revealed that the amino group on b-PEI would change to an ammonium group when blended with MAI due to the strong basicity of amino group (pK_a of ~10; the pK_a of pyridine is ~5). The protonation of b-PEI could potentially change the interactions from a coordination-type bonding (amino-Pb^{2+}) to ionic bonding ($CH_3NH_3^+$-I^-). Thereafter, although passivation effect is observed with amino group (*64*), the formation of ionic bonding might introduce trap states due to the electron-withdrawing effect of ammonium to I^-, which weakens the I–Pb bond. Further investigation is needed to find the detailed mechanism.

Another challenging issue with perovskite solar cells is their stability. By introducing a small cross-linking molecule, Li *et al.* (*45*) demonstrated high device performance with high stability. Ideally, a polymer cross-linker would be more effective in reinforcing the stability of the perovskite film. However, the strategy of using polymers for efficient passivation and crystal cross-linking is limited by processing because the strong interaction between the electron-donating groups and the perovskite precursors makes it difficult to form a smooth film. Therefore, only polymers with weak interactions with the perovskite have been incorporated in previous studies (*65*, *66*). Using a mesoporous scaffold–facilitated interdiffusion method, we have successfully incorporated polymers with different functional groups into the films. The mesoporous PbI_2 films were developed via slow growth, and the polymers along with MAI were interdiffused into the pores of the PbI_2 film, forming a coordination bond with the perovskite crystals during crystallization. Above all, by incorporating the optimal coordinating polymer (PVP) into the perovskite film, the perovskite solar cells reverse-scanned device efficiency improves to 20.2% (18.8 ± 0.8%; stabilized efficiency of 19.1%; under bias of 0.94 V and AM 1.5-G, 1-sun illumination for 30 min) and the shelf time stability to more than 3 months (retaining 85% of the original efficiency).

MATERIALS AND METHODS

Materials

The MAI iodide was home-synthesized, and the lead iodide was purchased from Alfa Aesar and was used as received. The Spiro-OMeTAD was purchased from Lumitech Corp. and was used as received. Other materials not specified were from Sigma-Aldrich.

Device fabrication

The patterned ITO glass substrates were cleaned using an ultrasonicator in an acetone, water, and IPA bath. A SnO_2 layer was formed on the surface of the ITO substrate. $SnCl_2 \cdot 2H_2O$ was dissolved in ethanol (11 mg ml^{-1}) in a vial and aged by vigorously stirring for 1 hour at room temperature and ambient atmosphere, leaving the vial uncapped. The $SnCl_2$ solution was spin-coated twice on ITO glass at 3000 rpm for 30 s. A SnO_2 thin film with an approximate thickness of 30 nm was formed after annealing the spin-coated film in ambient atmosphere at 150°C for 30 min and 180°C for 60 min. After cooling at room temperature, the glass/ITO/SnO_2 substrates were transferred into an ultraviolet-ozone cleaner for 15 min and then left in a dry-air glove box. The perovskite films were deposited by a sequential two-step solution process. Hot PbI_2 solution (600 mg/ml; in dimethylformamide) was spun onto the glass/ITO/SnO_2 substrates at 3000 rpm for 40 s. For fabrication of mesoporous PbI_2, the samples were taken out from the spin coater after 20 s and left in a petri dish for 15 min. After annealing on a 75°C hot plate for 15 min, the mesoporous PbI_2 substrates were dripped with MAI/MACl solution (70:7 mg/ml; in IPA) by spin-coating to form the PbI_2-MAI complex films. The complex films were put on a 135°C hot plate for 15 min. The Spiro-OMeTAD solution [80 mg/ml; in chlorobezene with 3% 4-tert-butylpyridine and 9 mg of lithium bis(trifluoromethanesulfonyl)imide] was spun onto the perovskite film as a hole conductor. The devices were completed by evaporating 80-nm gold in a vacuum chamber (base pressure, 5×10^{-4} Pa).

Device characterization

The device efficiencies were measured using a Keithley SourceMeter under AM 1.5-G, 1-sun irradiance, as generated by a thermo oriel solar simulator. The light intensity was adjusted by a KG-5 Si diode, which can be traced back to the National Renewable Energy Laboratory. The devices were measured in ambient air at temperature of 22°C. Different scan directions (reverse scan, from 1.2 to –0.2 V; forward scan, from 0 to 1.2 V) were recorded at a scan rate of 0.5 V/s for the hysteresis study. The device pixel had the dimension of 0.2 cm by 0.7 cm, and the accurate device area was defined by an aperture of 0.1031 cm^2. The device photocurrent showed little variation with the aperture area. In addition, for the steady-state output measurement, the solar cells were put under the simulated AM 1.5-G, 1-sun illumination to record the photocurrent under the bias of 0.88 and 0.94 V. The EQE was measured on an Enlitech measurement system. The shelf lifetime of the devices was measured in ambient air (relative moisture, 20 to 40%; temperature, 20° to 25°C) and by storing them in a N_2 glove box.

TPV decay measurements

A white light bias was generated from an array of diodes (Molex 180081-4320) to simulate a 1-sun working condition. A pulsed red dye laser (rhodamine 6G; 590 nm) pumped by a nitrogen laser (LSI VSL-337ND-S) was used as the perturbation source, with a pulse width of 4 ns and a repetition frequency of 10 Hz. The perturbation light intensity was attenuated to keep the amplitude of transient V_{OC} (ΔV_{OC}) below 5 mV so that $\Delta V_{OC} << V_{OC}$. Voltage dynamics were recorded on a digital oscilloscope (Tektronix DPO4104B), and voltages at open circuit were measured over a megohm and a 50-ohm resistor, respectively.

PL and TRPL measurements

A Horiba Jobin Yvon system with a red-light source with an excitation at 640 nm was used to conduct PL measurements. TRPL spectra were obtained using a PicoHarp 300 with time-correlated single-photon counting capabilities. A picosecond diode laser provided excitation at a wavelength of 640 nm with a repetition frequency of 1 MHz (PDL 800B).

Scanning electron microscopy

An emission Nova 230 NanoSEM was used to obtain SEM images with an electron beam acceleration in the range of 500 V to 30 kV.

FTIR spectra

The FTIR spectra (4000 to 500 cm^{-1}) were recorded on a Jasco FT/IR-6100 FTIR with samples prepared on silicon substrates.

Electronic IS measurement

IS measurements were performed using the Hewlett Packard 4284A Precision LCR Meter providing voltage modulation in the desired frequency range. The running program was edited with MATLAB R2003. The Z-view software (v2.8b, Scribner Associates Inc.) was used to analyze the impedance data. The IS experiments were performed at a constant temperature of 20°C under illumination with various intensities. The impedance spectra of the perovskite devices were recorded at potentials in the range of $V_{OC} \pm 0.1$ V at frequencies ranging from 20 Hz to 1 MHz, the oscillation potential amplitudes being adjusted to 30 mV. The ITO electrode was used as the working electrode, and the Au electrode (CE) was used as both the auxiliary electrode and the reference electrode.

DFT simulation

Our first-principles calculations were carried out using the Vienna ab initio simulation package (VASP) (*67*), a DFT approach using the projector-augmented wave method (*68*, *69*). Calculations were performed using the Perdew-Burke-Ernzerhof version of the generalized gradient approximation (*70*) for exchange correlation. Surface slabs were modeled as (001)-terminated slabs of tetragonal structure. In our calculation, eight asymmetric interchanging MAI-PbI_2 monolayers with 30 Å vacuum added on top of the slab surface were used. Dipole slab correction was applied to remove artificial dipole-dipole interaction across periodic images in VASP. To demonstrate the passivation effect of polymers of different functional groups, we concentrated on the PbI_2-terminated surface because its surface energy is small (*37*). Adsorption energies were calculated using

$$E_{ads} = E(\text{functional groups} + \text{slab}) - E(\text{slab}) \\ - E(\text{functional group})$$

GDOES measurement

Depth-dependent compositional profiles were collected with a Horiba GD-Profiler 2 using a high-power radio frequency argon plasma in a 4-mm-diameter anode. The plasma was operated at 30 W and a pressure of 450 Pa. Oxygen (O) and lead (Pb) were detected using the 130- and 406-nm atomic emission lines, respectively.

^{1}H NMR

The ^{1}H NMR spectra were recorded in solution of dimethyl sulfoxide–d6 on a Bruker DRX300 NMR spectrometer with tetramethylsilane as the internal standard.

SUPPLEMENTARY MATERIALS

Supplementary material for this article is available at http://advances.sciencemag.org/cgi/content/full/3/8/e1700106/DC1

fig. S1. Interactions between the perovskite precursors (PbI_2 and MAI) and polymers.

fig. S2. FTIR spectra of perovskite (PVSK), polyethylenimine (PEI), and perovskite/polyethylenimine (PVSK + PEI) films.

fig. S3. GDOES (O element) of perovskite films processed and measured under the same condition.

fig. S4. Surface morphology of perovskite films.

fig. S5. XRD patterns of perovskite film with and without different polymers.

fig. S6. *I-V* characteristic curves of perovskite solar cells with PVP grain boundary passivation.

fig. S7. EQE spectra of perovskite solar cells versus photon energy.

fig. S8. *I-V* characteristic of perovskite solar cells with different amount of PVP.

fig. S9. *I-V* characteristic of perovskite solar cells (made from compact PbI_2) with and without PVP.

fig. S10. Histogram of device efficiency distribution of perovskite solar cells with different polymers.

fig. S11. *I-V* hysteresis behavior of perovskite solar cells with and without different polymer passivation.

fig. S12. Depth-dependent PL behavior of perovskite film with or without PVP.

fig. S13. A typical Nyquist plot for a PVP device at an open-circuit voltage under 1-sun illumination in the frequency range of 20 Hz to 1 MHz.

fig. S14. Binding energy–dependent device performance.

fig. S15. Interactions between MAI and the polymers.

REFERENCES AND NOTES

1. N.-G. Park, Perovskite solar cells: An emerging photovoltaic technology. *Mater. Today* **18**, 65–72 (2015).
2. G. Hodes, Perovskite-based solar cells. *Science* **342**, 317–318 (2013).
3. S. D. Stranks, H. J. Snaith, Metal-halide perovskites for photovoltaic and light-emitting devices. *Nat. Nanotechnol.* **10**, 391–402 (2015).
4. J. Seo, J. H. Noh, S. I. Seok, Rational strategies for efficient perovskite solar cells. *Acc. Chem. Res.* **49**, 562–572 (2016).
5. Y. Bai, Q. Dong, Y. Shao, Y. Deng, Q. Wang, L. Shen, D. Wang, W. Wei, J. Huang, Enhancing stability and efficiency of perovskite solar cells with crosslinkable silane-functionalized and doped fullerene. *Nat. Commun.* **7**, 12806 (2016).
6. H.-S. Kim, C.-R. Lee, J.-H. Im, K.-B. Lee, T. Moehl, A. Marchioro, S.-J. Moon, R. Humphry-Baker, J.-H. Yum, J. E. Moser, M. Grätzel, N.-G. Park, Lead iodide perovskite sensitized all-solid-state submicron thin film mesoscopic solar cell with efficiency exceeding 9%. *Sci. Rep.* **2**, 591 (2012).
7. A. Kojima, K. Teshima, Y. Shirai, T. Miyasaka, Organometal halide perovskites as visible-light sensitizers for photovoltaic cells. *J. Am. Chem. Soc.* **131**, 6050–6051 (2009).
8. H. Zhou, Q. Chen, G. Li, S. Luo, T.-b. Song, H.-S. Duan, Z. Hong, J. You, Y. Liu, Y. Yang, Interface engineering of highly efficient perovskite solar cells. *Science* **345**, 542 (2014).

9. L. Zuo, Z. Gu, T. Ye, W. Fu, G. Wu, H. Li, H. Chen, Enhanced photovoltaic performance of $CH_3NH_3PbI_3$ perovskite solar cells through interfacial engineering using self-assembling monolayer. *J. Am. Chem. Soc.* **137**, 2674–2679 (2015).
10. C.-C. Chueh, C.-Z. Li, A. K.-Y. Jen, Recent progress and perspective in solution-processed Interfacial materials for efficient and stable polymer and organometal perovskite solar cells. *Energ. Environ. Sci.* **8**, 1160–1189 (2015).
11. L. Zuo, Q. Chen, N. De Marco, Y.-T. Hsieh, H. Chen, P. Sun, S.-Y. Chang, H. Zhao, S. Dong, Y. Yang, Tailoring the interfacial chemical interaction for high-efficiency perovskite solar cells. *Nano Lett.* **17**, 269–275 (2017).
12. N. J. Jeon, J. H. Noh, Y. C. Kim, W. S. Yang, S. Ryu, S. I. Seok, Solvent engineering for high-performance inorganic–organic hybrid perovskite solar cells. *Nat. Mater.* **13**, 897–903 (2014).
13. Q. Chen, H. Zhou, Z. Hong, S. Luo, H.-S. Duan, H.-H. Wang, Y. Liu, G. Li, Y. Yang, Planar heterojunction perovskite solar cells via vapor-assisted solution process. *J. Am. Chem. Soc.* **136**, 622–625 (2014).
14. M. Liu, M. B. Johnston, H. J. Snaith, Efficient planar heterojunction perovskite solar cells by vapour deposition. *Nature* **501**, 395–398 (2013).
15. J. Burschka, N. Pellet, S.-J. Moon, R. Humphry-Baker, P. Gao, M. K. Nazeeruddin, M. Grätzel, Sequential deposition as a route to high-performance perovskite-sensitized solar cells. *Nature* **499**, 316–319 (2013).
16. G. E. Eperon, V. M. Burlakov, P. Docampo, A. Goriely, H. J. Snaith, Morphological control for high performance, solution-processed planar heterojunction perovskite solar cells. *Adv. Funct. Mater.* **24**, 151–157 (2014).
17. L. Zuo, S. Dong, N. De Marco, Y.-T. Hsieh, S.-H. Bae, P. Sun, Y. Yang, Morphology evolution of high efficiency perovskite solar cells via vapor induced intermediate phases. *J. Am. Chem. Soc.* **138**, 15710–15716 (2016).
18. N. J. Jeon, J. H. Noh, W. S. Yang, Y. C. Kim, S. Ryu, J. Seo, S. I. Seok, Compositional engineering of perovskite materials for high-performance solar cells. *Nature* **517**, 476–480 (2015).
19. D. P. McMeekin, G. Sadoughi, W. Rehman, G. E. Eperon, M. Saliba, M. T. Hörantner, A. Haghighirad, N. Sakai, L. Korte, B. Rech, M. B. Johnston, L. M. Herz, H. J. Snaith, A mixed-cation lead mixed-halide perovskite absorber for tandem solar cells. *Science* **351**, 151–155 (2016).
20. D. Bi, W. Tress, M. I. Dar, P. Gao, J. Luo, C. Renevier, K. Schenk, A. Abate, F. Giordano, J.-P. C. Baena, J.-D. Decoppet, S. M. Zakeeruddin, M. K. Nazeeruddin, M. Grätzel, A. Hagfeldt, Efficient luminescent solar cells based on tailored mixed-cation perovskites. *Sci. Adv.* **2**, e1501170 (2016).
21. M. Saliba, T. Matsui, J.-Y. Seo, K. Domanski, J.-P. Correa-Baena, M. K. Nazeeruddin, S. M. Zakeeruddin, W. Tress, A. Abate, A. Hagfeldt, M. Grätzel, Cesium-containing triple cation perovskite solar cells: Improved stability, reproducibility and high efficiency. *Energ. Environ. Sci.* **9**, 1989–1997 (2016).
22. W. E. I. Sha, X. Ren, L. Chen, W. C. H. Choy, The efficiency limit of $CH_3NH_3PbI_3$ perovskite solar cells. *Appl. Phys. Lett.* **106**, 221104 (2015).
23. W. L. Leong, Z.-E. Ooi, D. Sabba, C. Yi, S. M. Zakeeruddin, M. Graetzel, J. M. Gordon, E. A. Katz, N. Mathews, Identifying fundamental limitations in halide perovskite solar cells. *Adv. Mater.* **28**, 2439–2445 (2016).
24. Q. Wang, Q. Dong, T. Li, A. Gruverman, J. Huang, Thin insulating tunneling contacts for efficient and water-resistant perovskite solar cells. *Adv. Mater.* **28**, 6734–6739 (2016).
25. D.-Y. Son, J.-W. Lee, Y. J. Choi, I.-H. Jang, S. Lee, P. J. Yoo, H. Shin, N. Ahn, M. Choi, D. Kim, N.-G. Park, Self-formed grain boundary healing layer for highly efficient CH_3 NH_3 PbI_3 perovskite solar cells. *Nat. Energy* **1**, 16081 (2016).
26. M. L. Terry, A. Straub, D. Inns, D. Song, A. G. Aberle, Large open-circuit voltage improvement by rapid thermal annealing of evaporated solid-phase-crystallized thin-film silicon solar cells on glass. *Appl. Phys. Lett.* **86**, 172108 (2005).
27. J. B. Li, V. Chawla, B. M. Clemens, Investigating the role of grain boundaries in CZTS and CZTSSe thin film solar cells with scanning probe microscopy. *Adv. Mater.* **24**, 720–723 (2012).
28. A. W. Tsen, L. Brown, M. P. Levendorf, F. Ghahari, P. Y. Huang, R. W. Havener, C. S. Ruiz-Vargas, D. A. Muller, P. Kim, J. Park, Tailoring electrical transport across grain boundaries in polycrystalline graphene. *Science* **336**, 1143–1146 (2012).
29. N. H. Nickel, N. M. Johnson, W. B. Jackson, Hydrogen passivation of grain boundary defects in polycrystalline silicon thin films. *Appl. Phys. Lett.* **62**, 3285–3287 (1993).
30. D. W. deQuilettes, S. M. Vorpahl, S. D. Stranks, H. Nagaoka, G. E. Eperon, M. E. Ziffer, H. J. Snaith, D. S. Ginger, Impact of microstructure on local carrier lifetime in perovskite solar cells. *Science* **348**, 683–686 (2015).
31. J. S. Yun, J. Seidel, J. Kim, A. M. Soufiani, S. Huang, J. Lau, N. J. Jeon, S. I. Seok, M. A. Green, A. Ho-Baillie, Critical role of grain boundaries for ion migration in formamidinium and methylammonium lead halide perovskite solar cells. *Adv. Energy Mater.* **6**, 1600330 (2016).
32. Y. Shao, Y. Fang, T. Li, Q. Wang, Q. Dong, Y. Deng, Y. Yuan, H. Wei, M. Wang, A. Gruverman, J. Shield, J. Huang, Grain boundary dominated ion migration in polycrystalline organic–inorganic halide perovskite films. *Energ. Environ. Sci.* **9**, 1752–1759 (2016).
33. J.-J. Li, J.-Y. Ma, Q.-Q. Ge, J.-S. Hu, D. Wang, L.-J. Wan, Microscopic investigation of grain boundaries in organolead halide perovskite solar cells. *ACS Appl. Mater. Interfaces* **7**, 28518–28523 (2015).
34. J.-P. Correa-Baena, M. Anaya, G. Lozano, W. Tress, K. Domanski, M. Saliba, T. Matsui, T. J. Jacobsson, M. E. Calvo, A. Abate, M. Grätzel, H. Míguez, A. Hagfeldt, Unbroken perovskite: Interplay of morphology, electro-optical properties, and ionic movement. *Adv. Mater.* **28**, 5031–5037 (2016).
35. M. Yang, Y. Zeng, Z. Li, D. H. Kim, C.-S. Jiang, J. van de Lagemaat, K. Zhu, Do grain boundaries dominate non-radiative recombination in $CH_3NH_3PbI_3$ perovskite thin films? *Phys. Chem. Chem. Phys.* **19**, 5043 (2017).
36. Q. Chen, H. Zhou, T.-B. Song, S. Luo, Z. Hong, H.-S. Duan, L. Dou, Y. Liu, Y. Yang, Controllable self-induced passivation of hybrid lead iodide perovskites toward high performance solar cells. *Nano Lett.* **14**, 4158–4163 (2014).
37. J. Haruyama, K. Sodeyama, L. Han, Y. Tateyama, Termination dependence of tetragonal $CH_3NH_3PbI_3$ surfaces for perovskite solar cells. *J. Phys. Chem. Lett.* **5**, 2903–2909 (2014).
38. F. Matteocci, Y. Busby, J.-J. Pireaux, G. Divitini, S. Cacovich, C. Ducati, A. Di Carlo, Interface and composition analysis on perovskite solar cells. *ACS Appl. Mater. Interfaces* **7**, 26176–26183 (2015).
39. W. Geng, C.-J. Tong, Z.-K. Tang, C. Y. Yam, Y.-N. Zhang, W.-M. Lau, L.-M. Liu, Effect of surface composition on electronic properties of methylammonium lead iodide perovskite. *J. Materiomics* **1**, 213–220 (2015).
40. N. K. Noel, A. Abate, S. D. Stranks, E. S. Parrott, V. M. Burlakov, A. Goriely, H. J. Snaith, Enhanced photoluminescence and solar cell performance *via* Lewis base passivation of organic–inorganic lead halide perovskites. *ACS Nano* **8**, 9815–9821 (2014).
41. D. W. deQuilettes, S. Koch, S. Burke, R. K. Paranji, A. J. Shropshire, M. E. Ziffer, D. S. Ginger, Photoluminescence lifetimes exceeding 8 μs and quantum yields exceeding 30% in hybrid perovskite thin films by ligand passivation. *ACS Energy Lett.* **1**, 438–444 (2016).
42. Y. Shao, Z. Xiao, C. Bi, Y. Yuan, J. Huang, Origin and elimination of photocurrent hysteresis by fullerene passivation in $CH_3NH_3PbI_3$ planar heterojunction solar cells. *Nat. Commun.* **5**, 5784 (2014).
43. J. Xu, A. Buin, A. H. Ip, W. Li, O. Voznyy, R. Comin, M. Yuan, S. Jeon, Z. Ning, J. J. McDowell, P. Kanjanaboos, J.-P. Sun, X. Lan, L. N. Quan, D. Ha Kim, I. G. Hill, P. Maksymovych, E. H. Sargent, Perovskite–fullerene hybrid materials suppress hysteresis in planar diodes. *Nat. Commun.* **6**, 7081 (2015).
44. B. Chaudhary, A. Kulkarni, A. K. Jena, M. Ikegami, Y. Udagawa, H. Kunugita, K. Ema, T. Miyasaka, Poly(4-vinylpyridine)-based interfacial passivation to enhance voltage and moisture stability of lead halide perovskite solar cells. *ChemSusChem* **10**, 2473–2479 (2017).
45. X. Li, M. I. Dar, C. Yi, J. Luo, M. Tschumi, S. M. Zakeeruddin, M. K. Nazeeruddin, H. Han, M. Grätzel, Improved performance and stability of perovskite solar cells by crystal crosslinking with alkylphosphonic acid ω-ammonium chlorides. *Nat. Chem.* **7**, 703–711 (2015).
46. M. E. Ziffer, J. C. Mohammed, D. S. Ginger, Electroabsorption spectroscopy measurements of the exciton binding energy, electron–hole reduced effective mass, and band gap in the perovskite $CH_3NH_3PbI_3$. *ACS Photonics* **3**, 1060–1068 (2016).
47. M. Saliba, T. Matsui, K. Domanski, J.-Y. Seo, A. Ummadisingu, S. M. Zakeeruddin, J.-P. Correa-Baena, W. R. Tress, A. Abate, A. Hagfeldt, M. Grätzel, Incorporation of rubidium cations into perovskite solar cells improves photovoltaic performance. *Science* **345**, 206–209 (2016).
48. N. F. Curtis, Macrocyclic coordination compounds formed by condensation of metal-amine complexes with aliphatic carbonyl compounds. *Coord. Chem. Rev.* **3**, 3–47 (1968).
49. T. Suksrichavalit, S. Prachayasittikul, C. Nantasenamat, C. Isarankura-Na-Ayudhya, V. Prachayasittikul, Copper complexes of pyridine derivatives with superoxide scavenging and antimicrobial activities. *Eur. J. Med. Chem.* **44**, 3259–3265 (2009).
50. Z. Xiao, C. Bi, Y. Shao, Q. Dong, Q. Wang, Y. Yuan, C. Wang, Y. Gao, J. Huang, Efficient, high yield perovskite photovoltaic devices grown by interdiffusion of solution-processed precursor stacking layers. *Energ. Environ. Sci.* **7**, 2619–2623 (2014).
51. T. Liu, Q. Hu, J. Wu, K. Chen, L. Zhao, F. Liu, C. Wang, H. Lu, S. Jia, T. Russell, R. Zhu, Q. Gong, Mesoporous PbI_2 scaffold for high-performance planar heterojunction perovskite solar cells. *Adv. Energy Mater.* **6**, 1501890 (2016).
52. M. B. Huglin, J. M. Rego, Study of polymer blends based on poly(vinylpyridines) and acidic polymers. *Polymer* **31**, 1269–1276 (1990).
53. J. L. Velada, L. C. Cesteros, I. Katime, Infrared study of the interactions between poly(vinyl pyridines) and poly(mono-*n*-alkyl itaconates). *Appl. Spectrosc.* **50**, 893–899 (1996).
54. T. Nelis, J. Pallosi, Glow discharge as a tool for surface and interface analysis. *Appl. Spectrosc. Rev.* **41**, 227–258 (2006)
55. B. Chen, M. Yang, S. Priya, K. Zhu, Origin of *J–V* hysteresis in perovskite solar cells. *J. Phys. Chem. Lett.* **7**, 905–917 (2016).
56. C. Eames, J. M. Frost, P. R. F. Barnes, B. C. O'Regan, A. Walsh, M. S. Islam, Ionic transport in hybrid lead iodide perovskite solar cells. *Nat. Commun.* **6**, 7497 (2015).
57. Y. Zhang, M. Liu, G. E. Eperon, T. C. Leijtens, D. McMeekin, M. Saliba, W. Zhang, M. de Bastiani, A. Petrozza, L. M. Herz, M. B. Johnston, H. Linb, H. J. Snaith, Charge selective contacts, mobile ions and anomalous hysteresis in organic–inorganic perovskite solar cells. *Mater. Horiz.* **2**, 315–322 (2015).

58. J. M. Azpiroz, E. Mosconi, J. Bisquert, F. De Angelis, Defect migration in methylammonium lead iodide and its role in perovskite solar cell operation. *Energ. Environ. Sci.* **8**, 2118–2127 (2015).
59. S. D. Stranks, G. E. Eperon, G. Grancini, C. Menelaou, M. J. P. Alcocer, T. Leijtens, L. M. Herz, A. Petrozza, H. J. Snaith, Electron–hole diffusion lengths exceeding 1 micrometer in an organometal trihalide perovskite absorber. *Science* **342**, 341–344 (2013).
60. L. M. Herz, Charge-carrier dynamics in organic-inorganic metal halide perovskites. *Annu. Rev. Phys. Chem.* **67**, 65–89 (2016).
61. G. E. Eperon, D. Moerman, D. S. Ginger, Anticorrelation between local photoluminescence and photocurrent suggests variability in contact to active layer in perovskite solar cells. *ACS Nano* **10**, 10258–10266 (2016).
62. X. Xu, Z. Liu, Z. Zuo, M. Zhang, Z. Zhao, Y. Shen, H. Zhou, Q. Chen, Y. Yang, M. Wang, Hole selective NiO contact for efficient perovskite solar cells with carbon electrode. *Nano Lett.* **15**, 2402–2408 (2015).
63. M. Wang, P. Chen, R. Humphry-Baker, S. M. Zakeeruddin, M. Grätzel, The influence of charge transport and recombination on the performance of dye-sensitized solar cells. *ChemPhysChem* **10**, 290–299 (2009).
64. S. Lee, J. H. Park, B. R. Lee, E. D. Jung, J. C. Yu, D. Di Nuzzo, R. H. Friend, M. H. Song, Amine-based passivating materials for enhanced optical properties and performance of organic–inorganic perovskites in light-emitting diodes. *J. Phys. Chem. Lett.* **8**, 1784–1792 (2017).
65. Y. Zhao, J. Wei, H. Li, Y. Yan, W. Zhou, D. Yu, Q. Zhao, A polymer scaffold for self-healing perovskite solar cells. *Nat. Commun.* **7**, 10228 (2016).
66. Y. Guo, K. Shoyama, W. Sato, E. Nakamura, Polymer stabilization of lead(II) perovskite cubic nanocrystals for semitransparent solar cells. *Adv. Energy Mater.* **6**, 1502317 (2016).
67. G. Kresse, J. Furthmüller, Efficient iterative schemes for ab initio total-energy calculations using a plane-wave basis set. *Phys. Rev. B* **54**, 11169–11186 (1996).
68. P. E. Blöchl, Projector augmented-wave method. *Phys. Rev. B* **50**, 17953–17979 (1994).
69. G. Kresse, D. Joubert, From ultrasoft pseudopotentials to the projector augmented-wave method. *Phys. Rev. B* **59**, 1758–1775 (1999).
70. J. P. Perdew, K. Burke, M. Ernzerhof, Generalized gradient approximation made simple. *Phys. Rev. Lett.* **77**, 3865–3868 (1996).

Acknowledgments: We thank C. Wang for the DFT calculation and X. Shi for ^{1}H NMR measurement. **Funding:** This work was financially supported by a grant from the Office of Naval Research (grant no. N000141110250), University of California, Los Angeles (UCLA) Internal Funds, UC-Solar Program (fund number MRPI 328368), China Scholarship Council (No. 201506165038), and the Enli Tech (Taiwan) for donating the EQE measurement system to UCLA. **Author contributions:** L.Z. conceived the ideas, rationalized the experiments, performed the data analysis, and prepared the manuscript. H.G. conducted the device fabrication and measurement. S.D. measured the PL. R.D. and B.D. measured the FTIR spectroscopies. N.D. performed the SEM measurement. D.W.D., S.J., and D.S.G. helped with the GDOES measurement and data analysis on PL. M.W. carried out the *C-V*, TPV, and TPC measurements and analyzed the data. Y.Y. guided and supervised the whole study. All authors discussed the results and commented on the manuscript. **Competing interests:** The authors declare that they have no competing interests. **Data and materials availability:** All data needed to evaluate the conclusions in the paper are present in the paper and/or the Supplementary Materials. Additional data related to this paper may be requested from the authors.

Submitted 10 January 2017
Accepted 1 August 2017
Published 23 August 2017
10.1126/sciadv.1700106

Citation: L. Zuo, H. Guo, D. W. deQuilettes, S. Jariwala, N. De Marco, S. Dong, R. DeBlock, D. S. Ginger, B. Dunn, M. Wang, Y. Yang, Polymer-modified halide perovskite films for efficient and stable planar heterojunction solar cells. *Sci. Adv.* **3**, e1700106 (2017).